Neural network based process coupling and parameter upscaling in reactive transport simulations

Nikolaos I. Prasianakis [a,*], Robin Haller [a,b], Mohamed Mahrous [a,b],
Jenna Poonoosamy [c], Wilfried Pfingsten [a], Sergey V. Churakov [a,b]

[a] *Laboratory for Waste Management, Paul Scherrer Institut, CH-5232 Villigen PSI, Switzerland*
[b] *University of Bern, Institute of Geological Sciences, CH-3012 Bern, Switzerland*
[c] *Institute of Energy and Climate Research (IEK-6): Nuclear Waste Management and Reactor Safety, Forschungszentrum Jülich GmbH, 52425 Jülich, Germany*

Abstract

The multiscale modelling of geochemical processes requires efficient couplings between scales and physics. The use of machine learning techniques and neural networks has the potential to systematically improve the accuracy of models at acceptable computational costs. In this paper, we discuss an efficient framework to transfer information between multi-physics models across spatial scales. In the first example, we train a shallow neural network based on the results of micro-scopic geochemical reactive transport simulations, and integrate it in a Darcy-scale reactive transport code. In the second example, we train a neural network on geochemical speciation data produced from dedicated geochemical solvers, and adapted to the needs of a lab-on-a-chip microfluidic experiment, in order to accelerate the geochemical calculations. The reactive transport simulation benchmarks show that the neural network approach performs better than the full speciation reactive transport simulations or the look up table-based approaches, both in terms of computational efficiency and memory requirements. Based on these results we discuss the advantages and drawbacks of each simulation approach as well as the potential for further development of the modelling algorithms.
© 2020 Elsevier Ltd. All rights reserved.

1. INTRODUCTION

Geochemical reactions and coupled mass- and heat-transport are primary driving forces of geochemical processes occurring at various subsurface systems, such as the natural geothermal reservoirs and the technical geo-engineering systems. The latter include deep and subsurface geothermal energy exploitation systems, enhanced oil recovery, carbon dioxide capture sequestration, and disposal of radioactive waste. In these systems, the geochemical equilibrium is disturbed by the contrast in chemical composition of the injected fluids, or by the chemical disequilibrium between the materials used for construction of technical barriers and the surrounding geological formations.

It is very common, that the geochemical equilibration processes in such systems will result in the dissolution and precipitation of minerals, which in turn modify the transport properties of materials, such as porosity, permeability, diffusivity, as well as the subsurface stress fields. Quantitative prediction of time dependent in situ conditions in such systems is challenging not only due to the complexity of the chemistry and of the heterogeneous microstructure, but

* Corresponding author.

E-mail address: nikolaos.prasianakis@psi.ch (N.I. Prasianakis).

also because of non-linear coupling between processes at very different temporal and spatial scales (Churakov and Prasianakis, 2018). Macroscopically observed chemical and transport phenomena are strongly related to the processes that take place at the pore and the atomistic scale. The diffusion of solutes and solvent is the result of the thermal motion of individual molecules. Within porous media the transport of solutes is further affected by the interaction with the mineral surfaces, the pore connectivity and the pore geometry (Churakov and Gimmi, 2011; Churakov et al., 2014; Yang et al., 2019, 2020). The kinetics of mineral dissolution and replacement reactions are controlled by the supply of reactants to, and the removal of reaction products from, the mineral surface and the intrinsic surface reactivity. The macroscopically measured reaction kinetics is thus an interplay of mass transport and surface reactivity (Kurganskaya and Churakov, 2018). Scale specific models and simulation concepts, e.g. atomistic scale, pore level, repository level, are well established and mature (Steefel et al., 2015). The same holds for geochemical modeling software tools as for example PHREEQC (Parkhurst and Appelo, 1999) and GEMS (Kulik et al., 2013a). However, the complexity and range of the involved scales and processes requires multiscale and multiphysics couplings. Presently, it is not possible to incorporate all scales and processes involved in a typical geochemical system, in a single code. A multiscale simulation approach has to be based on the efficient transfer of necessary information across different scales and across different modelling tools. This task is in practice cumbersome, since there are no standard interfaces between codes or between different computer architectures.

To obtain deeper process understanding and to elucidate the role of couplings between distinct physical and chemical phenomena, dedicated experiments need to be combined with thermodynamic and reactive transport modelling. According to the characteristic length scale, experiments and simulations can be categorized for example into microfluidic (Soulaine et al., 2017; Poonoosamy et al., 2019), core scale (Molins et al., 2012; Bijeljic et al., 2013; Gray et al., 2018), and field scale (Wersin et al., 2004; Kosakowski and Berner, 2013; Steefel et al., 2015; Hubbard et al., 2018). It is common that the field scale simulations (Darcy-scale) use a simplified description of the processes that actually take place at the pore-level scale (microscale). For example, the effect of geochemical reactions in the permeability and the diffusivity of a porous medium is correlated to a global change of the bulk porosity in the medium using empirical relationships. It has been demonstrated, that smooth simplified relations are frequently inadequate to predict accurately the temporal evolution of the system of interest (Steefel et al., 2015). The predictability of the models can be greatly improved after resolving experimentally and numerically the physical phenomena and the process mechanisms occurring at the microscale, followed by an upscaling procedure to the Darcy-scale (Noiriel and Daval, 2017; Deng et al., 2018; Prasianakis et al., 2018).

A robust coupling between geochemical reactions at the pore-level and the field scale reactive transport simulations can be established via effective porosity–permeability correlations (Molins and Knabner, 2019). Through these correlations, the macroscopic code can be aware of the underlying physics and of the effect of the geochemical reactions at the pore scale, which are sensitive to the reaction rates, the flow regimes, and the composition of the fluids. For example, depending on chemical conditions and characteristic Damköhler number, a calcite rock can be dissolved following a face dissolution mechanism or via wormhole mechanism (Hoefner and Fogler, 1988; Portier et al., 2009; Menke et al., 2016). The resulting porosity–permeability correlation for the same rock depends on the reactive environment and can be greatly different (Prasianakis et al., 2018).

For a geochemically reactive transport problem, in addition to the solution of the advective–diffusive flow field, the chemical reactions and resulting chemical speciation at each grid point, and at every time step have to be considered. To resolve the transient system evolution, and depending on the simulated physical time and the selected timestep, these calculations at every grid point have to be repeated several thousand times.

For realistic system descriptions, the chemical reactions and speciation calculations are the parts of the algorithms that consume most of the computational time, when compared to the time needed for the mass transport calculations. Lately, there has been a number of efforts to accelerate geochemical calculations, as well as the full reactive transport calculations, using machine learning techniques and data-driven surrogate models, especially when sensitivity analysis are conducted (Asher et al., 2015; Jatnieks et al., 2016; De Lucia et al., 2017; Leal et al., 2017a, 2017b; Shen et al., 2018; Laloy and Jacques, 2019; Guérillot and Bruyelle, 2020). Similar techniques have been applied in the past in the field of reactive flows relevant to combustion (Christo et al., 1996). A primary target of these developments is the reduction of the computational overhead for geochemical calculation, by replacing the full geochemical calculations with a more compact low dimensional data-driven model. This results in faster but less accurate computations. In (Jatnieks et al., 2016) several machine learning methods ranging from random forest techniques to neural networks have been compared in a geochemically reactive transport setup. The authors identified the neural-network based techniques as the most promising ones. In Laloy and Jacques (2019) the authors compare machine learning techniques for emulating full reactive transport models, for a sensitivity analysis and uncertainty propagation, relevant to the desorption of uranium U(VI) from radionuclide contaminated sediments. Among other, they compare the efficiency of deep neural networks and highlight advantages and disadvantages of different simulation strategies. In a recent work, Guérillot and Bruyelle (2020), used also artificial neural networks, which are trained during runtime, to calculate the geochemical equilibrium instead of the actual geochemical solver.

In this paper, we use machine learning and more specific the training of artificial neural networks, (a) for upscaling the effect of geochemical reactions and reactive transport occurring at the micrometer scale to the macroscopic scale,

and (b) for accelerating geochemical calculations in a cross-scale reactive transport model. The first example is relevant to the calcite dissolution in low pH conditions (Prasianakis et al., 2018). The output of fully resolved geochemically reactive pore-level simulations is expressed in terms of porosity permeability correlations and used as input to a macroscopic reactive transport code. For that, a single hidden layer neural network is trained and the comparison with closed form correlations in a high reactivity regime is shown. In the second example, we focus on the modelling of a heterogeneous celestine precipitation experiment that is conducted on a lab-on-a-chip reactor (Poonoosamy et al., 2019). Chemical speciation during runtime is then computed with several techniques ranging from exact geochemical calculations to lookup tables and to training of deep-neural networks. The accuracy and efficiency of these techniques is assessed using a demanding complex two dimensional lab-on-a-chip reactor, where the interplay of the advective flow, the diffusive flow and the precipitation kinetics, dictate the evolution of the geochemical system.

2. METHODS

2.1. Pore-level and macroscopic modelling

The pore-level simulations applied in this work are based on the lattice Boltzmann method (LBM). The multi-component reactive transport model, which is used here, has been presented in (Safi et al., 2017b; Prasianakis et al., 2018; Curti et al., 2019). The lattice Boltzmann method (LBM) is a special discretization of the Boltzmann equation operating at the level of velocity probability distribution functions f_i, with focus on fluid dynamics and mass and heat transport phenomena. Applications of LBM range from diffusion dominated reactive transport simulations in porous media (Kang et al., 2002; Heuveline and Krause, 2010; Prasianakis et al., 2013; Chopard et al., 2015; Patel et al., 2017, 2018), to multiphase fluid dynamics of turbulent flow (Succi, 2001; Chen et al., 2003). For the model considered here, the primary solute species are transported via advection and diffusion. The fluid advective flow field is calculated by a single component LB model (basis fluid), which recovers the Navier-Stokes equations at the macroscopic limit. The solutes are then transported by advection and diffusion along the streamlines of the flow as passive scalars. The isothermal guided equilibrium model is used for the collision process (Prasianakis et al., 2017; Molins et al., 2020). This model provides enhanced Galilean invariance and rotational isotropy on the standard two-dimension nine velocity (D2Q9) and three dimension twenty-seven velocity lattices (D3Q27) (Prasianakis and Karlin, 2008; Prasianakis et al., 2009). Some strengths of the LBM, which are not exclusive for this method, for reactive transport geochemical applications are the ability to simulate evolving geometries of high complexity (due to dissolution or precipitation), the local mass and momentum conservation, as well as the parallelization efficiency. The high scalability of LBM codes is related to the locality of operations of the mesh based particle–particle interactions,

and the requirement of only next neighbor communication between the grid points during the streaming step. Macroscopic simulations of flow and mass transport at Darcy-scale were performed with the MCOTAC (Modular Coupling Of Transport And Chemistry) code. The coupling of solutes and transport along with the geochemical interactions is implemented using the sequential operator splitting approach. The code uses the law of mass action to calculate the aqueous speciation and the thermodynamic or kinetic equilibrium with single component solid phases. The diffusive transport of aqueous species is implemented using a random walk simulation algorithm. The changes in the permeability and diffusivity of the porous media due to the changes of porosity related to dissolution and precipitation of minerals are taken into account via effective Archie and Kozeny-Carman relations (Montoya et al., 2020; Pfingsten, 2002; Jakob et al., 2009).

Both numerical solvers have also participated in numerical benchmark exercises together with several state-of-the-art geochemically reactive transport codes (Montoya et al., 2020; Molins et al., 2020). The methodologies presented here are not restricted to the lattice Boltzmann and MCOTAC codes, but are in principle applicable to any combination of codes with similar functionality.

2.2. Thermodynamic speciation and LMA solver

Major computational efforts in reactive transport simulations are related to the calculations of thermodynamic equilibrium and the geochemical speciation. The reason for that is the large number of involved species, and the need to perform chemical calculations at each mesh point and every time step. Geochemical speciation calculations are used to find the quantities of chemical species in the system under the assumption of local equilibrium. This type of calculations can be done using the Law of Mass Action (LMA) (as in PhreeqC (Parkhurst, 1995)) or Gibbs Energy Minimization (GEM) (as in GEMS-Selektor). In a reactive transport code, reactions and mass transport are usually coupled in three main ways: by directly implementing the chemical speciation routines within the code (Xu et al., 2011), by using a pre-calculated look-up table that contains speciation calculations (Huang et al., 2018; Poonoosamy et al., 2019), or for more complex chemical systems by coupling the mass transport code to an external geochemical software (Kosakowski and Watanabe, 2014; Patel et al., 2017). The look-up table approach is in general faster but requires the pre-calculation of the full geochemical system, and the accuracy depends on the resolution of the table. On the other hand a direct calculation solving the chemical system will give an exact result, but it will be slower. For the second example presented in this paper, an exact LMA solver tailored for geochemical system of interest was embedded into the LBM code, and was used to obtain the exact fluid speciation at each time step of the reactive transport simulations.

The Law of Mass Action (LMA) simply states that the rate of chemical reaction is directly proportional to the product of the activities of the reactants raised to the power of their stoichiometric coefficients. At chemical equilibrium,

the LMA transfers to equilibrium constant (Keq) equations, given by:

$$K_i = \prod_{j=1}^{n} \gamma_j^{v_{ij}} c_j^{v_{ij}} \tag{1}$$

where K_i is the equilibrium constant of ith reaction, v_{ij} is the stochiemetric coefficient of jth species in ith reaction (positive for products and negative for reactants), c_j is the concentration of jth species, n is the total number of species, and γ_j is the activity coefficient of jth species, calculated in the exact LMA implementation using the Davies equation, given by;

$$\log_{10}\gamma_j = -AZ_j^2 \left(\frac{\sqrt{I}}{1+\sqrt{I}} - 0.3I \right) \tag{2}$$

where A is a temperature dependent constant equals to 0.5114 at 25 °C and 1 bar, I is the ionic strength. To achieve closure of the system of equations, the LMA equations are complemented by Mass Balance (MB) equations. Table 1 lists the chemical system along with its LMA and MB equations, where square brackets are for concentrations and curly brackets for the activities.

For a given aqueous speciation, the saturation index of celestine mineral is calculated using;

$$SI_{celestine} = \log_{10} \frac{\{Sr^{+2}\}\{SO_4^{-2}\}}{K_{sp}} \tag{3}$$

where $\{Sr^{+2}\}$ and $\{SO_4^{-2}\}$ are the activities of strontium and sulphate ions respectively and K_{sp} is the solubility product constant of celestine.

The speciation calculations with the exact LMA solver were first validated against the open-source GEM-Selektor V3.4.2. (Kulik et al., 2013a). GEM-Selektor is a geochemical modeling software that uses Gibbs Energy Minimization to model various geochemical processes, including batch speciation calculations. The agreement between the LMA solver and GEMS geochemical speciation was excellent for the whole range of concentrations.

2.3. Artificial neural networks

Artificial neural networks (NN) are computational models that can represent complex relationships between input and output data in multidimensional spaces (Jain et al., 1996). Different NN's types are assembled to exhibit specific behavior depending on their architecture, and the type of the problem to be solved. The main challenge of machine learning algorithms is to sufficiently train a NN using an existing training set of input and output data, such that the NN can be used to forecast accurate output values for data that do not belong to the training dataset. At the same time, it should be noted that a trained NN is not a direct human interpretable object, because of its high complexity compared, for example, with polynomial closed form expressions. Moreover, there is no optimum predefined number of neurons or an a-priori guarantee that a trained NN with a specific number of neurons can predict the output with the desired accuracy.

The feedforward type of neural networks are used in this study. This is one of the simplest but most efficient network type, suitable for solving complex regression problems. In this study the neural networks were trained using a supervised learning approach in order to: (a) transfer effective simulation parameters between microscopic and macroscopic simulations codes, and (b) approximate the exact geochemical speciation algorithms.

The neural network used for the approximation of geochemical speciation is depicted in Fig. 1. This network consists of an input, an output and two hidden layers composed by eight neurons per layer. For this example, the network accepts two variables as input, which are the master chemical species of interest and one variable as output, which is the resulting saturation index. A layer in the NN is capable of solving the following expression:

$$y = a(wx + b) \tag{4}$$

where x is the input matrix, w are the weights, b are biases, y is the calculated target vector and a is the activation or transfer function. For the output layer, $a = 1$, while for a hidden layer, a is equal to a function like e.g. the logistic or the tanh function. Thus, one or more hidden layers enable the nonlinear regression of the NN. For this specific example where we have two hidden layers in addition to the default output layer, y is calculated as follows:

$$y = a^3(w^3 * a^2(w^2 * a^1(w^1 * x + b^1) + b^2) + b^3) \tag{5}$$

Table 1
List of primary and secondary species along with its corresponding law of mass action and mass balance equations for a $SrCl_2$–Na_2SO_4 System.

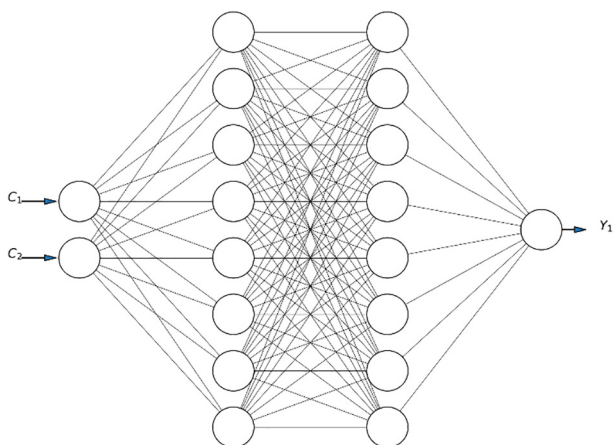| Primary Species	Secondary Species	LMA and MB Equations
1. Sr_{total}	**1. Sr^{2+}**	1. $Sr^{2+} + SO_4^{2-} \leftrightarrow SrSO_{4(aq)}$ $K_{eq1} = \{SrSO_{4(aq)}\}/\{Sr^{2+}\}\{SO_4^{2-}\}$ **(LMA.1)**
2. S_{total}	**2. SO_4^{2-}**	2. $Na^+ + SO_4^{2-} \leftrightarrow NaSO_4^-$ $K_{eq2} = \{NaSO_4^-\}/\{Na^+\}\{SO_4^{2-}\}$ **(LMA.2)**
3. Na_{total}	**3. $SrSO_{4(aq)}$**	3. $Sr_{total} = [Sr^{2+}] + [SrSO_{4(aq)}]$ **(MB.1)**
4. Cl_{total}	**4. $NaSO_4^-$** **5. Na^+** **6. Cl^-**	4. $S_{total} = [SO_4^{2-}] + [NaSO_4^-] + [SrSO_{4(aq)}]$ **(MB.2)** 5. $Na_{total} = [Na^{2+}] + [NaSO_4^-]$ **(MB.3)** 6. $Cl_{total} = [Cl^-]$ **(MB.4)**

Fig. 1. Visualization of the feedforward neural network used for the geochemical speciation example. This NN has two hidden layers composed by eight neurons per layer. This NN accepts two variables as input (e.g. master species concentrations $C_1 = [Sr^{2+}]$ and $C_2 = [SO_4^{2-}]$) and predicts one variable Y_1 (the saturation index of celestine) as output.

The superscripts 1 and 2 correspond to the hidden layers, while 3 denotes the output layer, which means $a^3 = 1$. For a^1 and a^2, the activation function tanh was chosen, which means e.g. for the first layer

$$a^1\left(w^1 * x + b^1\right) = \frac{\left(e^{w^1 * x + b^1} - e^{-(w^1 * x + b^1)}\right)}{\left(e^{w^1 * x + b^1} + e^{-(w^1 * x + b^1)}\right)} \tag{6}$$

Each neuron in a layer of a neural network can be seen as a pair of weights w and a bias b, whose values are determined during the training of the NN. The number of weights per neuron corresponds to the number of rows in x. In a layer, b corresponds to a vector whose size is equal to the number of neurons, while w is a matrix whose size is determined by the number of neurons and either the dimension of the input or the number of neurons in the previous layer. Among several choices, the training of the networks was conducted using the Neural Network Toolbox™ of MATLAB. It is noted that other alternative highly efficient open-source libraries can also be used, especially when the training process needs to be automated and has to occur during runtime in high performance computing clusters (Abadi et al., 2016).

At the beginning of the training, w and b are set to zero or random numbers, therefore after one training run (epoch) the predicted vector y and the true data t will be quite different. This difference is estimated via a mean squared error loss function

$$L = \frac{1}{n} \sum_{i=1}^{n} (t_i - y_i)^2 \tag{7}$$

where n is the total number of data points. Target of the training is the minimization of L, which will result in the lowest possible error of y compared to t. The NN training is using the backpropagation technique introduced by Rumelhart et al. (1986). In this method each weight w and bias b in the network is adjusted by calculating the partial derivative of L with w and b after each epoch.

The neural networks in this work were trained with the following procedure: The full data was randomly split into training, validation and testing with ratios of 70%, 15% and 15%, respectively. During training, the neural network adapts its parameters (weights and biases) only based on the training data. The validation data serves as a restriction to ensure that the NN can generalise well (i.e. it is able to reproduce unknown data) while the testing data is an additional independent dataset to control the quality of the neural network. The right balance between the size of the network and its resulting accuracy was pursued. For that, several networks were tested, by varying the number of neurons per hidden layer, the number of hidden layers and the activation functions of the neurons. Moreover, several training algorithms were tested. For datasets at hand, the best performing algorithm was found to be the one based on the Bayesian Regularization (see e.g. Mackay, 1992). Bayesian regularization enables smart adaption of regularizing parameters during training (Burden and Winkler, 2008; Kayri, 2016). To obtain a trained neural network with good generalization (low validation error), early stopping was used during training, which means that training stopped after the validation loss stopped decreasing. We note that a common issue in this type of networks is the element mass conservation between input and output of the networks, which cannot be guaranteed and which at the moment is source of uncertainty (Jatnieks et al., 2016; Guérillot and Bruyelle, 2020). For the example in Section 3.2, the mass conservation is guaranteed at the level of the multicomponent lattice Boltzmann implementation. While the SI is the driving force of precipitation small inaccuracies have no effect in mass conservation.

2.4. Lab-on-a-chip experiments

Lab-on-a-chip microfluidic reactive transport experiments have the potential to miniaturize several types of centimeter to meter laboratory experiments for several scientific disciplines. Some of the advantages of these microscale experiments are the requirements of small amount of reactants, the observation of processes occurring within confined micrometer size pores and interfaces, and the possibility of conducting several parallel experiments using only one chip (Song et al., 2014; Li et al., 2018; Soulaine et al., 2018; Poonoosamy et al., 2019). However, at the same time, the monitoring and control of the experiment becomes more complex and very sensitive to the setup and flow conditions. Moreover, the accurate interpretation of results requires local information that cannot be easily obtained via pure experimental techniques. Such information is the local flow velocities, the local chemical composition, the speciation, and the saturation index, at every location within the microchip and most importantly at the crystal-fluid interface. These quantities can be retrieved via complementary numerical diagnostics based on reactive transport modelling. Here, the experiment presented in (Poonoosamy et al., 2019) is considered as a test case for the simulations. The experiment is characterized by advective and diffusive mass transport, while the chemical reactions lead to strontium sulphate precipitation,

which alters the flow and the mass transport pathways. The experiment was designed to study the effects of solution supersaturation and flow conditions on mineral growth in confined spaces by using a simple chemistry and well-controlled chemical boundary conditions. The experimental setup, (chip depicted in Fig. 2a) consisted of a microfluidic reactor with two parallel supply channels of 77 μm width and 10 μm depth that were connected via fifty mixing chambers. The dimension of the mixing chambers were 60 μm length, 77 μm width and 1 μm depth. In the middle of the mixing chambers, pillars were placed with a distance of 600 nm apart from each other. The chip was fabricated using conventional PDMS (polydimethylsiloxane) on glass technique (Gruenberger et al., 2013). Equimolar (10 mM) solutions of $SrCl_2$ and Na_2SO_4 were injected at inlet 1 and 2, respectively, at a constant flow rate of 1000 nL min^{-1}. The advective and diffusive transport of the reacting solutes in the chambers triggered the precipitation of strontium sulphate ($SrSO_4$). The reactions in the chambers were moni-tored using optical microscopy. Fig. 2b shows four distinct processes observed subsequently in the mixing chamber: nucleation and appearance of the first crystallite, growth of crystals, clogging at the pillars and dissolution of the $SrSO_4$ crystals. The formation of the first crystallites occurred preferentially close to the middle of the reaction chambers, in the region of high super saturation. $SrSO_4$ nuclei grew forming flat euhedral rhombohedral crystals, intergrowing the pillars of the reactor chambers, and retaining the crystallographic orientation of the initial crystal. At the later stages, the growth of the $SrSO_4$ crystals was greatly affected by the local flow and mass transport conditions. The evolution of the system resulted in a complete clogging of the chamber obstructing the transport pathways between the upper compartment and lower compartment. As a result, the saturation dropped leading to a decrease in growth, followed by dissolution of the celestine crystals. The snapshot at T = 560 min is considered as the starting point for the simulations of the second test case.
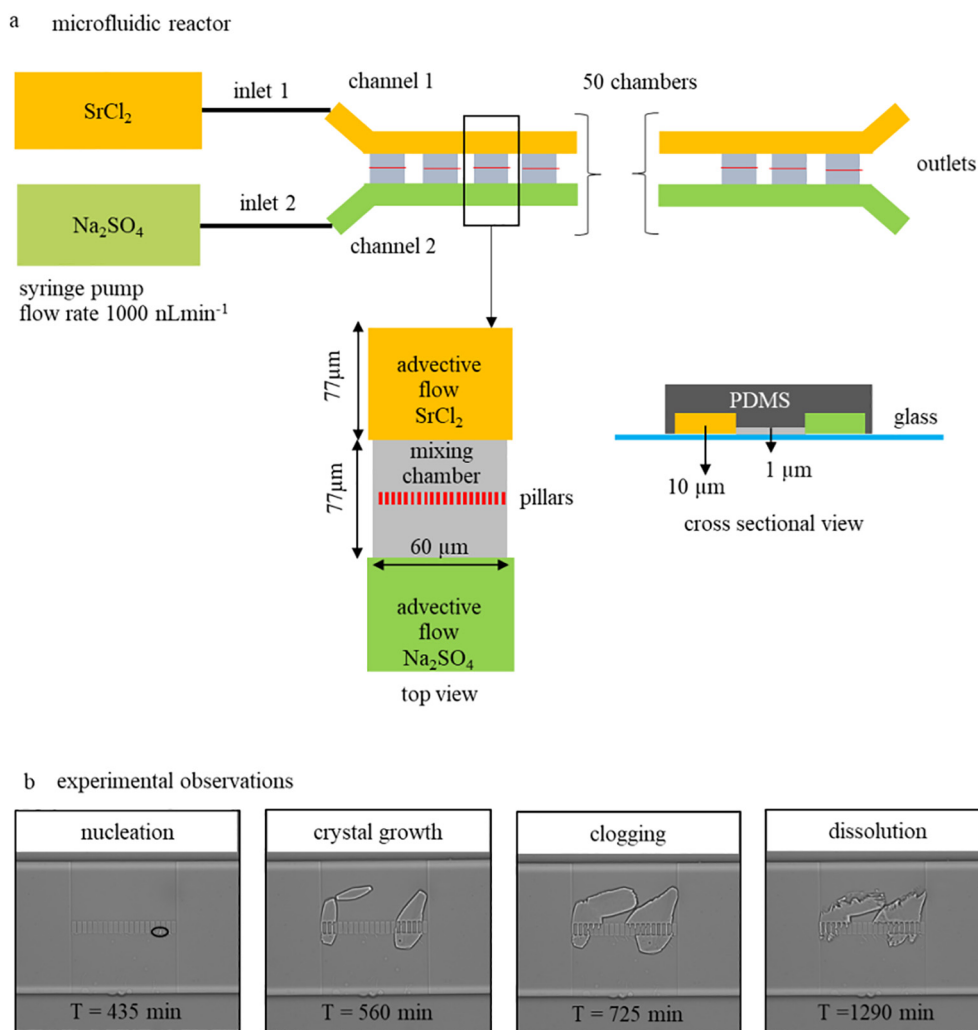

Fig. 2. (a) Schematic representation of the microchip experimental setup reported in (Poonoosamy et al., 2019) and (b) the observed temporal evolution in the mixing chamber (chamber number 4 from the inlet).

3. RESULTS

3.1. Transferring knowledge across the scales: effect of geochemical reactions on transport properties of porous materials

In macroscopic Darcy-scale models, the simulation domain is divided into grid cells that are equal to or larger than the "Representative Elementary Volume" (REV), defined as the minimum volume in which the physical parameters (pressure, density, porosity, etc.) are representative of the whole domain (Bear, 2013). Inside this REV, each phase is treated as a single continuum exhibiting properties that represent the statistical average of each macroscopic property within this volume. This averaging concept of the macroscopic scale models is double edged. While it allows modeling on large spatial scales with reasonable computational resources, it is insensitive to any micro scale changes that occur due to geochemical reactions, within the averaged grid cell.

Examples of these micro-scale changes due to geochemical reactions are the evolution of the pore network structure as a result of mineral precipitation and dissolution. The Darcy-scale models try to account for these reaction driven micro-scale changes by empirical relationships (Steefel et al., 2015) or coupling with lower scales models (Panga et al., 2005). For example, changes in the rock petrophysical properties such as permeability, reactive surface area, and diffusivity are assumed to be a function of porosity using empirical relationships such as Kozeny-Carman, power laws, and Archie's law. However, these empirical relationships tend to fail with increased chemical, mineralogical, and petrophysical heterogeneity due to the high non-linearity of the underlying microscopic reaction processes.

In microscopic models with explicit description of the pore structure and the reactive surfaces, the computational grid cells (or in this context, voxels) are no longer representative cells, and are explicitly defined as either rock- or pore- space. As a result of such a definition, the macroscopic properties of the rock such as the porosity, the permeability, and the effective diffusivity are not appearing in the mass transport and flow equations. At the same time some other parameters like the reactive surface area can be directly calculated from the explicitly resolved pore structure. Therefore, the reactive transport simulations at the microscopic pore-scale have the potential to elucidate the underlying mechanisms as well as to provide macroscopic codes with improved functions and relationships (Prasianakis et al., 2018). The main challenge in applying geochemically reactive transport models on realistic 3D porous geometries, is that such geometries require very fine discretization of the simulation domain, in order to resolve large and small pore-structures and their related reactive surfaces. If the geometry is composed from X-ray tomograms, it may result in computational domains with a very large number of voxels ($>10^9$) and massive computational costs. This limits the application of micrometer reactive transport models to small scale reactive transport experiments. However, at this level it is possible to describe very

interesting physical and geochemical mechanisms at very high resolution.

In Prasianakis et al. (2018) the result of geochemical reactions on the microstructure evolution of reacting porous media has been investigated via pore scale lattice Boltzmann simulations. The modelled system was represented by a calcite rock which was dissolved because of the injection of an acidic fluid. Simulations were conducted using computer generated synthetic pore maps, which were constructed based on the Voronoi tessellation method.

The coupling between flow conditions and reactivity at the pore-level is rationalized in terms of dimensionless parameters, such as the Peclet ($Pe = \text{UL/D}$), the Damköhler ($Da = \text{kL/D}$), and the Reynolds ($Re = \text{UL/v}$) numbers, where U is the convective flow velocity, L is the characteristic spatial dimension, D is the mass diffusivity, k is the reaction constant, and v is the kinematic viscosity of the fluid. These dimensionless numbers describe the interplay and significance of different geochemical and physical processes for a given system.

Depending on the reactant concentration and the flow rate, which results in different Pe, Da, and Re numbers, the geochemical reactions on the calcite rock led to distinct dissolution evolution paths. Different dissolution mechanisms were observed that ranged from face dissolution to wormhole formation. Different evolution paths resulted in different values of permeability for the same total dissolved calcite. Moreover, it was shown that in several cases the effective transport properties of the system significantly deviated from the typical Kozeny-Carman type of porosity–permeability correlations, which are usually used in macroscopic reactive transport codes. In Fig. 3 the pore level microscopic results are depicted for the case of $Pe = 400$ for initial porosity of $\varepsilon = 0.39$, which resulted in wormhole formation (Prasianakis et al., 2018). The Peclet number for the microscopic simulations is calculated by using the initial inflow velocity of the solution, the molecular diffusivity of the injected acid, and the characteristic length scale of the considered rock sample. We note that the Peclet definition at the pore-scale is different from the grid Peclet number used in macroscopic description, where the inflow velocity is correlated to the hydrodynamics dispersion coefficient (instead of only the molecular diffusion) and the dimension of the grid cell size (instead of characteristic length scale). After exhaustive search for a closed form fit, it was not possible to describe the underlying flow and dissolution processes with a single correlation, and therefore two correlations of permeability K, of the form $K = a * \varepsilon^b$ were adopted, namely:

$$K = 4.21 \cdot 10^{-17} \cdot \varepsilon^{2.4} \quad \text{for porosity} < 0.436 \text{ (mild regime)}$$
(8)

$$K = 4.89 \cdot 10^{-13} \cdot \varepsilon^{13.7} \quad \text{for } 0.436 < \text{porosity} < 0.48 \text{ (strong regime)}$$
(9)

These correlations are also plotted in Fig. 3 (left). The dataset produced from the pore-level detailed simulations was used as the input training data set for the neural network depicted in Fig. 3 (right). The selected neural network is a shallow network and includes one hidden layer with five
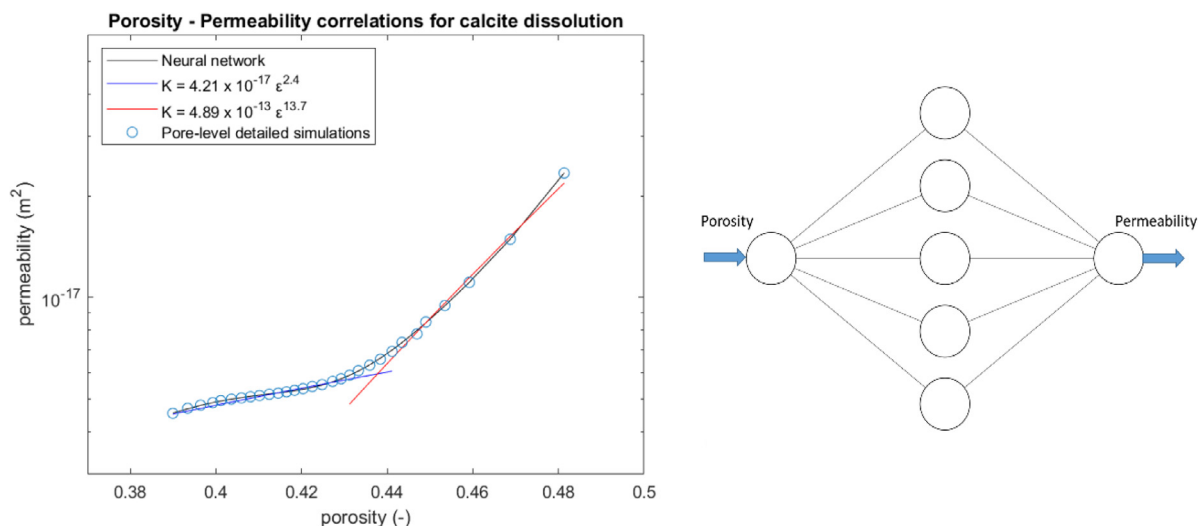
Fig. 3. (left) result of geochemical reactions on transport properties of porous media expressed as porosity permeability correlations. Circles represent the detailed pore-level lattice Boltzmann reactive transport simulations. The black line shows the trained neural network output. The blue (mild regime) and red (strong regime) lines represent the best two-step fit using closed form polynomial expressions of the type $\boldsymbol{K} = \boldsymbol{a} * \boldsymbol{\varepsilon}^{\boldsymbol{b}}$. (right). Topology of the shallow neural network (1 hidden layer, 5 neurons) which is trained using the pore level simulation dataset. (For interpretation of the references to colour in this figure legend, the reader is referred to the web version of this article.)

neurons. After the NN learning phase, the trained network was integrated in the macroscopic reactive transport code. The NN is capturing with excellent accuracy the trend of the permeability variation due to calcite dissolution. This is expected since a NN is a more complex mathematical model compared to the correlations of Eqs. (8) and (9). The same network architecture is also capable of capturing the trends resulting from the face dissolution mechanism.

The obtained knowledge of the phenomena that occur at the microscale can be further transferred to the macroscopic code, expressed as porosity permeability correlations. These correlations enclose the characteristic evolution of the rock properties due to geochemical reactions and mass transport. Here, we propose an alternative method based on neural networks, since the procedure of training can be fully automated within one and the same algorithm.

For the upscaling, the dissolution of calcite rock at the macroscopic scale is considered. The neural network was embedded into the macroscopic reactive transport code MCOTAC as a C function (also provided in the supplementary material file: porosity_permeability_NN_function.c) which could be used instead of a Kozeny-Carman or a power law porosity–permeability relationship. The MCOTAC code includes mineral precipitation and dissolution reactions, which yield porosity changes and related permeability and dispersivity/diffusivity changes. Different porosity–permeability relationships, as for example, simple Kozeny-Carman equation, polynomial equations or NN learned functions could be included via simple equations or functions calls. It is noted that neural network models are very robust and can be easily included into transport codes as embedded routine or external stand-alone library, which are not dependent on third-party libraries or on code packages. The discretization of the macroscopic simulation domain was on the cm scale

(from sub-micrometer at the pore-level scale), and the time scale is minutes and hours (from fractions of microseconds at the pore-level).

For the simulations, the boundary conditions were set similar to the conditions that resulted in the wormhole formation at the microscopic scale. The constant inflow condition (10^{-3} m/s) was used to fix a constant hydraulic head (h) boundary condition along the 1 meter long macroscopic model domain. For the outflow boundary condition (right) an infinite boundary condition is assumed along with a global hydraulic gradient which does not change with time. Therefore, the flow velocity v can be calculated from Darcy equation (Eq. (10)) for different 1D discretized model elements x_i:

$$v_i = \overrightarrow{v}_{Di}/\varepsilon_i = -k_i/\varepsilon_i \cdot grad\, h \qquad (10)$$

where v_{Di} is the Darcy velocity and k_i is the hydraulic conductivity, which is connected to the permeability K_i through the following relationship: $k_i = K_i g / v$, where g is the gravitational acceleration and v is the kinematic viscosity of the fluid.

The calcite dissolution caused by the injection of HCl acid of 0.01 M (pH = 2) was modelled by an equilibrium dissolution reaction, i.e. the fastest dissolution rate for calcite, according to the following reaction mechanism

$$CaCO_3 + H^+ \rightarrow Ca^{2+} + HCO_3^-, \;\; \log K_s = -1.84 \qquad (11)$$
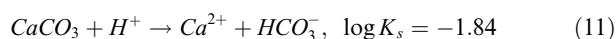
where $\log K_s$ is the solubility product constant. Pore water and calcite were initially set in equilibrium along the 1D model domain. The inflow of the HCl acid at the left boundary is reacting with the calcite causing its dissolution, and resulting in the alteration of the local porosity and permeability. Initial porosity was set to $\varepsilon = 0.39$ for all discrete elements.

For the simulations the two permeability-porosity power law correlations shown in Fig. 3, have been used. The first
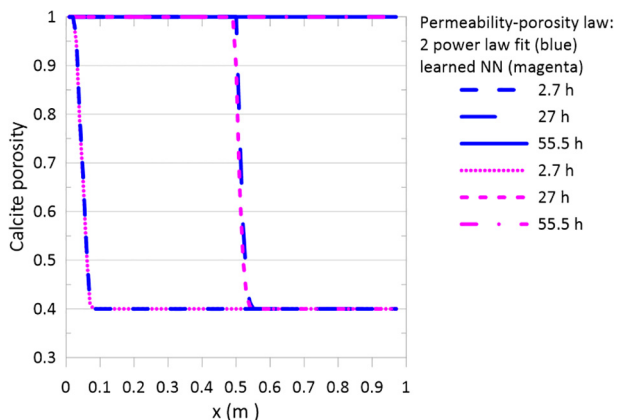
Fig. 4. Upscaling of the results of microscopic reactive transport simulations to macroscopic scale. Injection of HCL acid and calcite porosity distribution at different times along the model domain (100 grid cells). Two different permeability-porosity laws implemented in the macroscopic code (blue), and compared to the neural network approach (magenta). (For interpretation of the references to colour in this figure legend, the reader is referred to the web version of this article.)

correlation was applied for porosities less than $\varepsilon = 0.436$ (Eq. (8)) and the second correlation for porosities in the range $0.436 < \varepsilon < 0.48$ (Eq. (9)). For porosities >0.48, an upper limit in permeability was used. The maximum permeability was defined which is equal to the permeability calculated for the porosity of $\varepsilon = 0.48$. For simulations that implemented a neural network, the trained neural network model was used for porosities $0.39 < \varepsilon < 0.48$, and the same upper permeability limit for porosities >0.48, as used in the correlation based simulations. An equidistant grid was used, resulting to 100 internal domain grid cells (0.01 m cell size). Simulation results are shown Fig. 4. There is excellent agreement between the power laws and the neural network model implementations. At 27.2 h, half of the calcite rock is dissolved. After 55 hours of reaction time the entire calcite domain is dissolved. Different grid sizes were also tested
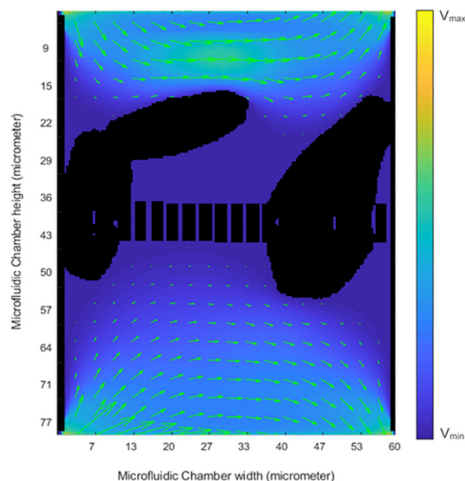

Fig. 5. Visualization of the flow field within the microfluidic chamber. Arrows depict the flow velocities and their relative magnitude. Reactants are transported at the fluid-crystal interface via advection and diffusion.

yielding very similar results. It is concluded that both methodologies can be used for transferring information across scales. Each methodology has its own advantages and drawbacks as described in the discussion section.

3.2. Accelerated cross-scale microfluidic simulation

The evolution of the lab-on-a-chip experiment presented in the Methods section is a result of several competing processes. In Fig. 5, a snapshot of the experiment at $T = 560$ min is depicted, along with the numerically resolved snapshot flow field (See Fig. 2b for the temporal evolution of the experiment). The velocity vectors indicate the local magnitude and direction of the flow at every point of the domain obtained by the cross scale LB solver. The multicomponent flow solver includes also a classical nucleation theory (CNT) implementation from which the induction time (time needed for the initiation of precipitation) and reactive surface areas are calculated (Prasianakis et al., 2017). Exact details of the calculation of the flow field within the chip have been presented in Poonoosamy et al. (2019). The reactants Na_2SO_4 and $SrCl_2$ enter from the left side of the domain (top and bottom) and are transported by advection and diffusion towards the pillar-zone in the middle of the chamber (see Fig. 9). At a certain distance from the pillar-zone, and depending on the crystal orientation and crystal extent, diffusion becomes the dominant transport mechanism. Reactants and products are carried away back to the channel, and exit the chamber from the right side. The mixing extends within the whole microfluidic chamber and results in a high contrast of the local species concentrations. In certain locations of the chamber, when the solubility limits are exceeded, and upon availability of appropriate substrate the celestine precipitation takes place. The kinetics of precipitation reaction dn/dt [mol s^{-1}] can be described by:

$$SrCl_{2(aq)} + Na_2SO_{4(aq)} \rightarrow SrSO_{4(s)} + 2\,NaCl_{(aq)},$$

$$\frac{dn}{dt} = S_A k^\circ \left(1 - \Omega^{0.5}\right)^2, \tag{12}$$

where $SI_{celestine} = \log_{10}\Omega$, S_A [m^2] is the reactive surface area of Celestine and, $k^\circ = 5.1 \times 10^{-8}$ [mol m^{-2}] according to Marty et al. (2015)). Due to the micrometer resolution, the reactive surface areas are directly available. Therefore, the precipitation rate is defined locally, and is dependent on the local conditions that apply exactly at each crystal-fluid reactive interface. For the conditions of the experiment, and for the resulting range of values of the saturation index, the induction time for homogeneous nucleation is infinitely long and only the heterogeneous nucleation is favored.

The evolution of the system is dictated by the local saturation index. The accurate prediction of the system evolution requires a full coupling between the flow and the chemical speciation. The calculation of the chemical speciation and of the local saturation index were integrated into the flow solver in three main different ways.

First, we have embedded in the LB algorithm the exact LMA solver, which provides accurate results for any combination of the reactant concentrations. Second, we have

created a lookup table using the same exact LMA solver, with a concentration resolution in log units, for the master species Sr^{2+} and SO_4^{2-}, ranging from [0.00001, 0.1] M in 40 equidistant steps (in log units). The resulting SI, after the calculation of the thermodynamic speciation was also stored in the lookup table. During runtime, a linear interpolation scheme was applied for the calculation of the approximate values of SI. Third, we trained a NN using as training input the aforementioned lookup table to allow a fair comparison between all methods. For the supervised learning, the strontium and sulphur concentrations were the two-dimensional input values, and SI was the output value. Only 70% of the lookup table data were used in a random way during the training process. The exact NN used is schematically shown in Fig. 1. The trained NN was programmed as a function with two inputs and one output and is provided in its benchmarking form in the supplemental material (file: nn8x8si.c). The performance of the NN

was quantified through the root of mean squared error (RMSE) which had the value of RMSE = $6.64 * 10^{-5}$ ($\log_{10}$ units).

For the purpose of numerical benchmarking, the simulations were initialized in the following way. First, the flow field was let to approach stationary state as depicted in Fig. 5, using the experimental snapshot at T = 560 min as a starting geometry. Second, the solutes were allowed to enter from the top and bottom left boundaries of the domain, which then advect and diffuse along the streamlines of the flow. Simulations run for $2.2 * 10^5$ timesteps corresponding to a period $\Delta t = 10$ seconds of real experimental time. At this timescale the reactants mix, mostly around the central zone with the pillars, and when the solubility limit of celestine is exceeded and after a short induction time (provided from the classical nucleation theory) the precipitation is initiated. The sequence of the evolution of the concentration field and of the SI are shown in Fig. 6. The concentra-
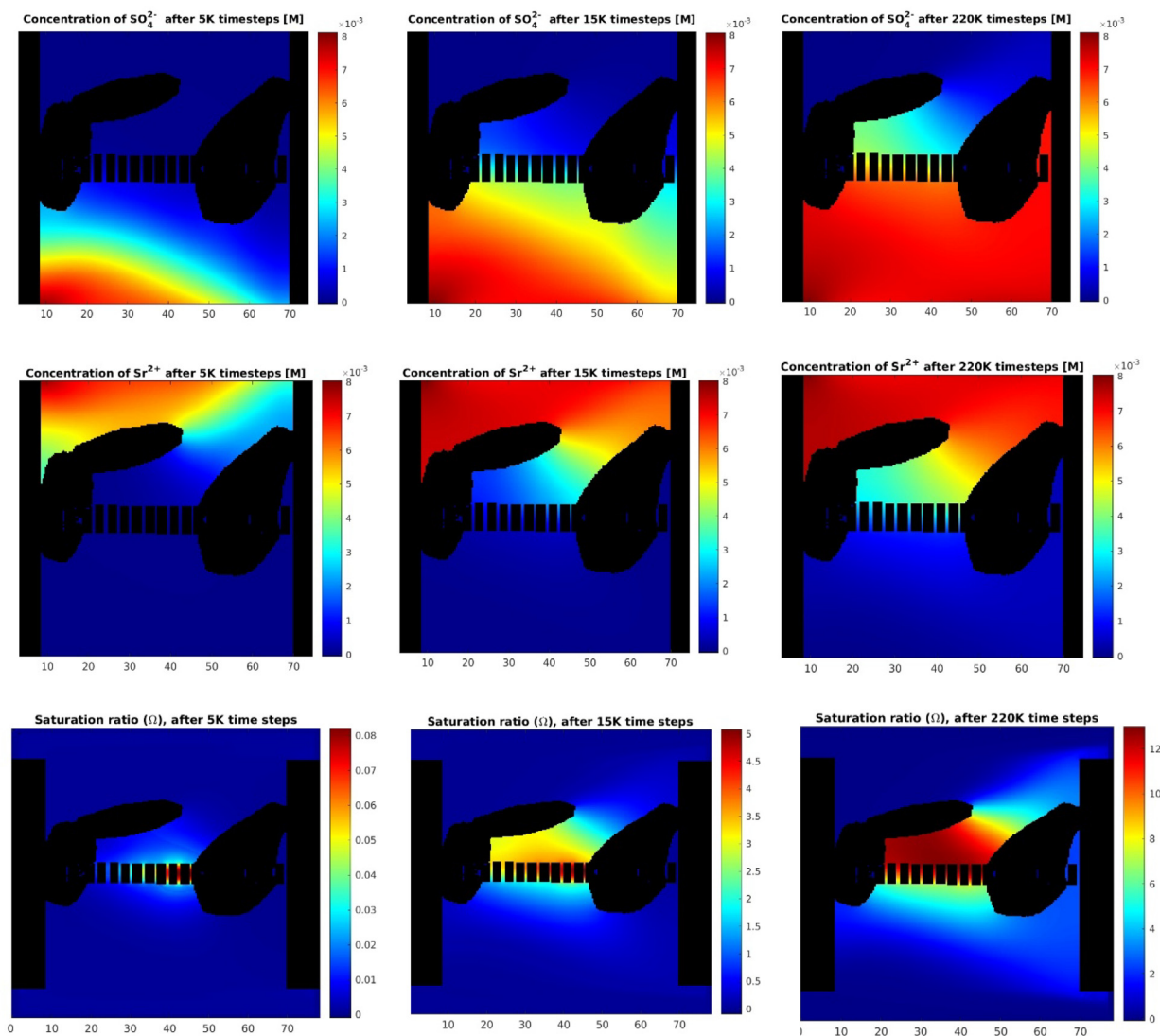

Fig. 6. First and second rows of plots shows the evolution of strontium and sulphur ion concentration for 5 K, 15 K and 220 K timesteps. 220 K timesteps correspond to $\Delta T = 10$ sec of real experimental time. The third row of plots shows the respective supersaturation with respect to celestine ($SI_{cel} = \log_{10}\Omega$). Numerical simulations can reveal information necessary for the interpretation of the experiments.

tion field is asymmetric and the saturation index varies. The precipitation zone, along the fluid-crystal interface, acts as a sink of Sr^{2+} and SO_4^{2-} ions. The competing transport and reaction mechanisms result in a quasi-stationary state in which, for the timeframe of $\Delta T = 10$ seconds, the system is reaching a constant global average saturation index, and a constant global precipitation rate. The stationary state is evolving at a relatively slow pace, along with the overgrowth of the celestine crystals, which can in turn subsequently affect the flow field. For the considered timeframe of $\Delta T = 10$ seconds the precipitated Celestine layers have a thickness much less than 1 µm (sub-lattice) and therefore the overgrowth is not significant to alter the flow field.

A comparison of the results of the simulations with the different geochemical coupling implementations is shown in Figs. 7–9. The exact LMA, the lookup table and the neural network implementation produce practically similar results and the differences for the quantities of interest are much below the uncertainties of the thermodynamic parameters, or the accuracy of the experimental measurement techniques. In Fig. 7 (left), the results of the lattice Boltzmann

cross-scale reactive transport simulations are shown for five different implementations. The coupling with the LMA solver is represented by a black solid curve. The lookup table implementation is shown with red squares, the result of NN's with blue circles (well trained network).

The results of an implementation of the same neural network using a very small learning rate and intentionally stopping before the training process is complete (insufficient training) are shown in green color. This is done mainly to demonstrate the importance of the learning process until the necessary accuracy is reached. Unsatisfactory training may result: when the selected knowledge base (training dataset) is very large leading to unrealistic training times followed by an early interruption of the learning process, because of inappropriate parametrization of the learning algorithm and activation functions, or due to overfitting. Moreover, we have linearly regressed the SI manifold and integrated the resulting function (plane) in the code. The results of linear regression, are shown as a red continuous line and as expected significantly deviate from the main three methods.
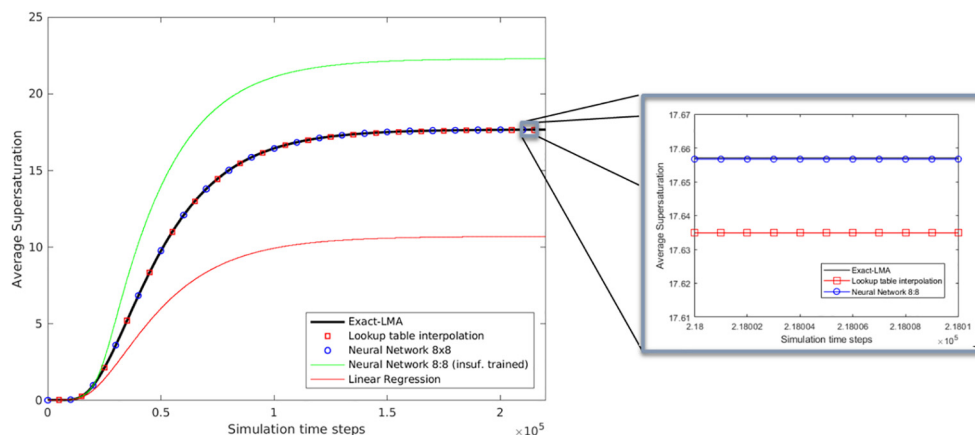

Fig. 7. Comparison of the evolution of the global saturation index (SI) for the transient lattice Boltzmann reactive transport simulation, for 220 K timesteps ($\Delta T = 10$sec). (left) Exact LMA, lookup table, NN (8x8 stands for 2 hidden layers with 8 nodes each) are in close agreement with each other. An incomplete trained NN is also shown in green color, and the result of linear regression in red color. (right) Zoom in at 218 K timestep. The NN is in closer agreement with the exact LMA, with a fourth decimal digit accuracy. (For interpretation of the references to colour in this figure legend, the reader is referred to the web version of this article.)
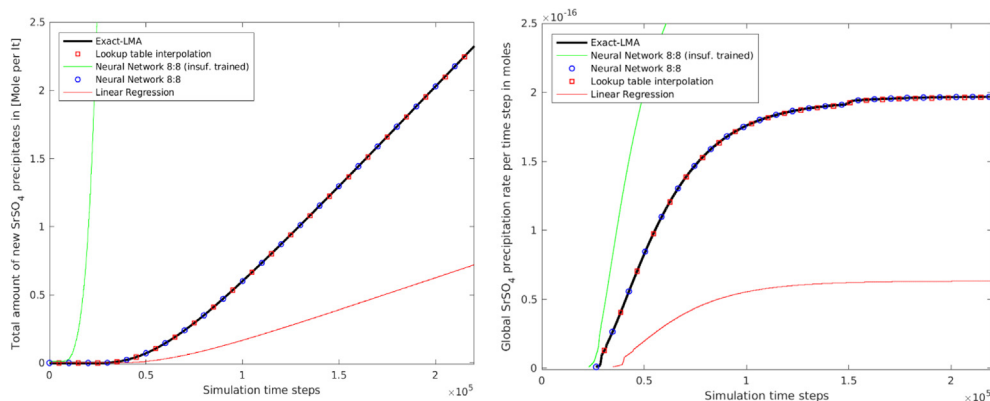

Fig. 8. Comparison of the different approaches for the full lattice Boltzmann reactive transport simulation, for 220 K timesteps ($\Delta T = 10$ sec). (left) Total amount of Celestine precipitates in mol per litre. An incomplete trained NN is also shown in green color, and the result of linear regression in red color. (right) Global celestine precipitation rate per timestep in moles within the microfluidic chamber. (For interpretation of the references to colour in this figure legend, the reader is referred to the web version of this article.)

The three main methodologies: exact LMA, lookup table and neural network implementation, are in very good agreement with each other. In Fig. 7 (right), the differences of these three methods are highlighted for the quasi-stationary state of T = 560 min + ΔT. The NN results are in much better agreement with the exact LMA solver, compared to the lookup table linear interpolation, and are able to reproduce the exact results within the fourth decimal digit. In Fig. 8 (left) the total amount of celestine precipitates is plotted for the different cases, while in Fig. 8 (right) the global precipitation rate per timestep is depicted. Considering computational efficiency, the exact LMA implementation had the slowest numerical performance, due to the high computational costs of the speciation calculations. The lookup table and the NN implementations were both significantly faster. Finally, in Fig. 9 a comparison between the exact LMA results and the result of the NN implementation shows the relative difference throughout the microfluidic chamber. In Fig. 9 (left) the map of the relative difference in percent for the local saturation index is shown. For that, at every location of the domain the SI is calculated first for the exact LMA implementation, and then is compared with the result of the well trained NN implementation. This highlights the excellent agreement and the accuracy of the NN implementation. The difference throughout the simulations, and even after 220 K timesteps, remains at very low levels and the system practically evolves in an identical way. The wavy form of the contour plot can be interpreted as the separation of regions of cumulative, over-prediction and under-prediction of the NN implementation.

A typical lattice Boltzmann code used for mass transport simulations can perform for a single component simulation around 5–10 million computational grid point updates per second, (million lattice updates per second MLUPS) on a single CPU core, or 400–1000 MLUPS on a GP-GPU device (Tölke and Krafczyk, 2008; Krüger et al., 2017; Safi et al., 2017a; Latt et al., 2020). A typical geochemical speciation code like GEMS or PHREEQC performs of the order of ~1000 geochemical calculations per second on a single CPU core (e.g Xeon E5-2650v4

2.2 GHz). Depending on the complexity of the chemical system performance can be slightly lower or higher. In the case of a direct coupling of the codes, for this reactive transport problem, where 4 master species are considered for advection and diffusion, the resulting code would spent 99.99% of the time for the geochemical speciation, since the flow and mass transport calculation is three to four orders of magnitude faster than the chemical reaction calculations.

The neural network used here, has a sustained throughput performance of ~13 million speciation calculations per second, measured on the same CPU core as above, thus giving a speed-up of four orders of magnitude compared to the geochemical speciation, with practically no loss in accuracy. In this case, the chemistry is not anymore the bottleneck. A C code that includes the neural network and the benchmark computation with all necessary information about the compiler options used for the efficiency measurement, can be found in the supplemental material (file: nn8x8si.c). This extreme speedup highlights the potential of using surrogate models and neural networks. We note that for more complex chemical systems, with more dimensions, larger networks will be required, thus reducing the throughput performance.

4. DISCUSSION

The physical and chemical processes observed in a typical experimental setup span over several length- and time-scales, making multi-scale modelling indispensable. The essence of the successful multiscale modelling approach is the efficient transfer of the parameters between models and codes operating at different scale. Such a granular description of the system enables us to focus on scale specific processes with an appropriate modelling approach.

4.1. Neural network models for scale and physics couplings

It can be argued that neural networks are black boxes without solid physical background to be applied for reactive transport calculations. Indeed, the resulting network in Fig. 1, cannot be rationalized in a simple hierarchy of
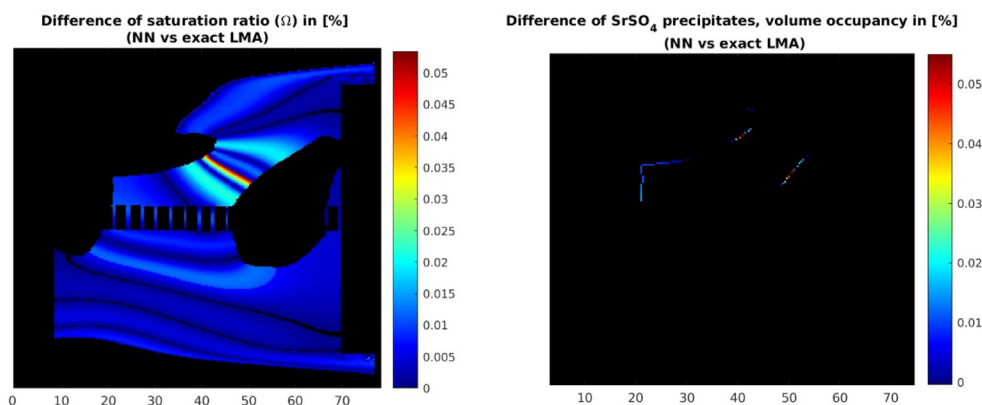

Fig. 9. Relative difference maps between the embedded exact LMA solver and the NN implementation after 220 K timesteps. (left) the difference in saturation ratio during the simulations remains throughout the domain at very low levels. The wavy form of the contour, after 220 K timesteps depicts regions of overprediction and underprediction. (right) The difference in percent of volume occupancy (per voxel) after 220 K timesteps remains also at very low levels.

models describing individual physical processes. The resulting mathematical model is a collection of double precision numbers, while the signal propagating between the input and the output nodes is processed by a network of neurons with a local short-range interaction. However, existing multi scale modelling concepts often also lack closed-form relationship between parameters that are obtained at different scales. The transferred parameters are interpolated using empirical polynomial relationships without a sound physical meaning.

The use of Kozeny-Carman type porosity–permeability correlations in reactive porous media, to upscale the result of geochemical reactive flow from the pore-scale to the Darcy-scale is a prominent example. Such relations seem to work well for slow dissolution/precipitation processes in a granular media with isomorphic shape of pores and mineral grains. At the same time, such correlations fail by several orders of magnitude to reproduce the system evolution in e.g. the case of fast calcite dissolution kinetics that result in a wormhole dissolution pattern. The same holds also in a scenario of mineral precipitation in porous media (Poonoosamy et al., 2020), where the correlations of porosity permeability deviate strongly from typical Kozeny-Carman. For example, under specific conditions of strong chemical gradients and fast reactions, a small change in the volume of precipitates within the considered control volume can result in strong reduction of the permeability and effective diffusivity and even to clogging (Churakov and Prasianakis, 2018). The example in Fig. 3 demonstrates that the numerical dataset obtained by reactive pore scale simulations, could not be accurately described by a single closed form correlation (power law). The best-fit functional form for the parameters correlations is a priori unknown, and depends on the flow and reaction conditions. The process of parameter fitting requires an educated guess of the functional form or an iterative supervision and thus cannot be easily automated or embedded in a multiscale algorithm.

Depending on the inflow velocity and the concentration of reactants prescribed by Pe, Da and Re numbers, the same geometry can follow a different permeability-porosity trajectory. For example, there exist experimentally and numerically produced phase diagrams of the different calcite rock dissolution regimes (Starchenko and Ladd, 2018; Seigneur et al., 2019). All such trajectories create a multi-dimensional permeability-porosity manifold where the dimensions are the initial porosity and the three non-dimensional numbers, which can eventually be represented by a trained neural network.

We also note that information can certainly be exchanged between codes and algorithms in a way similar to the lookup table interpolation presented in the chemical speciation example. Linear interpolation or spline interpolation should work equally well in the calcite dissolution example. However, such an approach cannot be generalized efficiently in higher dimensions, especially when the grid that is used for the interpolation is not regular/equidistant (e.g. scattered data points), which can be well the case when porosity–permeability relationship in the case of the aforementioned multidimensional manifold. The neural network models, on the other hand, have been successful in representing the arbitrary parameter dependencies and allow implementation of an automated training process (Miller et al., 1989; Yao, 1999).

4.2. Selection of optimum NN architecture, training and accuracy of neural networks

A crucial and controversially debated issue is related to the selection of the neural network topology and the NN dimensions (e.g. the number of hidden layer and the number of neurons per layer). To keep the computational efforts at minimum, both during the training and the use in numerical simulations, the smallest possible network is desirable. Depending on the application, the accuracy of shallow neural networks with few amount of neurons may be insufficient. Both shallow and deep neural networks are universal approximators. In general, adding more layers and neurons and moving from shallow NN to deep NN improves the NN accuracy, but may also result in an overfitting (Mhaskar and Liao, 2016). Overfitting can be addressed both by the training algorithms, as well as by adjusting the number of neurons. This was also observed in the case of the networks used for the acceleration of the geochemical speciation calculation. The available benchmarks suggest that the optimum network architecture has to be devised on a case-by-case basis.

In general, the time needed for the training is increasing with the number of nodes and layers and the amount of data used for the training. For the first benchmark of the upscaling of the geochemical reactions the full data consisted only by 31 data samples, and one second of training time was adequate. For the second example, relevant to the geochemical speciation, where 1600 data samples served as the full data, one minute of training was adequate to produce an accurate network. For more demanding trainings, e.g. due to more input/output variable, more hidden layers and neurons, the training can take several hours on a single cpu-core or some minutes in GPU/parallel setup.

A slightly more complex system is the system relevant to calcite dolomite dissolution precipitation. To represent the geochemical speciation a sample basis with primary variables the quantities of $CaCO_3$ and $MgCl_2$ in the range of -8 to 0 ($\log_{10}$ mol/l) and CO_2 in the range of -6 to -1.5 ($\log_{10}$ mol/l) as inputs, was created. The outputs of interest were eleven, which are the aqueous species $[Ca^{2+}]$, $[CaOH^+]$, $[Mg^{2+}]$, $[MgOH^+]$, $[CO_{2s}]$, $[CO_3^{2-}]$, $[HCO_3^-]$ in ($\log_{10}$ mol/l), the pe, the pH, and the solid phases of calcite and dolomite ($\log_{10}$ g/l). The generation of speciation data were produced with the open software GEM-Selektor, and were subsequently fed as training input for the neural network. It was trained with a total of 2890 datapoints, which spans a very coarse grid with a step size of 0.5 units in $\log_{10}$ space per input component. The neural network of Fig. 10 has 6 hidden layers with 14 neurons each. For a multidimensional output, the mean squared error loss function (Eq. (7)) is adapted to:

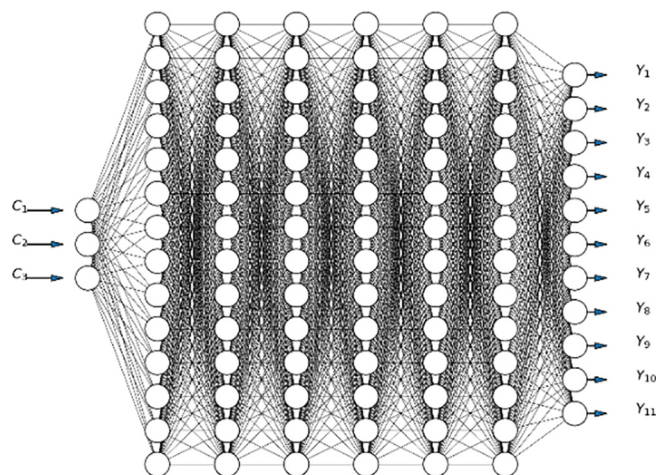$$L = \frac{1}{nd} \sum_{j=1}^{d} \sum_{i=1}^{n} (t_{i,j} - y_{i,j})^2, \tag{13}$$

Fig. 10. Visualization of the feedforward network used for the system with calcite and dolomite precipitation. It has six hidden layers with fourteen neurons per layer. The NN takes three components (C_1–C_3) as input and predicts eleven outputs (Y_1–Y_{11}).

where d is the dimension of the output. The network obtained a RMSE = $6.111 * 10^{-3}$. This accuracy has to be interpreted as the accuracy of the network to the knowledge that it was exposed. The obviously coarse grid that was used can only give a coarse representation of the underlying physics. For example when the network accuracy is tested on a much finer grid, its RMSE on the finer dataset is increased by two orders of magnitude. For a ten times finer grid with step size 0.05 units in $\log_{10}$ space, instead of 0.5 step size, the RMSE will be just 0.1095. When the NN is subsequently trained on the new knowledge (0.05 units in $\log_{10}$ space), its new RMSE for the new data reduces again to low levels. This process can go on, until the network becomes insensitive to finer resolutions. In this case the network converges to the behavior of the underlying physics as done in the case of the network used in Section 3.2. The network of Section 3.2 was trained using 70% of the 1600 samples of the lookup table and has an $RMSE_{1600} = 6.64 * 10^{-5}$, tested on the input data. To observe convergence to the underlying physics we have generated three independent data sets with 16′000, 160′000 and 15 Million random input data samples. The resulting errors relevant to the exact-LMA data were: $RMSE_{16K} = 7.1857 * 10^{-5}$, $RMSE_{160K} = 7.4027 * 10^{-5}$, $RMSE_{15M} = 7.45877 * 10^{-5}$, showing a clear convergence to very low levels of error.

A network of the size shown in Fig. 10 still has a throughput efficiency of 1–2 million speciation calculations per second on a single CPU core (see supplementary material file: calcite.c) , while the geochemical solver for this problem produces results at a pace of 300 speciation calculations per second.

Finally, it is noted that a NN is applicable for the specific problem, which was used to provide the training basis. Changes in the system (e.g. a new input component) requires a new training of the network. However, once the NN is trained at satisfactory accuracy, it can be reused for several applications and simulations. When the NN is not part of the pre-processing for a simulation, special care has to be taken for its quality assurance. For example a database composed of such NNs should also store the specifications of the chemical system, the exact version of the geochemical solver that was used to generate it and the relevant input.

4.3. Computational efficiency

The main motivation for using surrogate models is the expected increase in computational efficiency. A surrogate model can express the complex correlations between input and output data, without the need for a description of underlying physical mechanisms. On the other hand, for a single speciation calculation the geochemical algorithms have to find solutions in an iterative way until convergence. The number of iterations depends on the complexity of the system as well as on the relevant species concentrations. For a reactive transport code, the geochemistry is usually the bottleneck in terms of computational efficiency. In parallel reactive transport simulations, the geochemical speciation calculations are usually accomplished in parallel too. The convergence rate and the wall-clock time per geochemical speciation calculation with LMA or GEMs codes depend strongly (by several orders of magnitude) on the system composition. Such a variable performance raise a serious node balancing issue in massive parallel computing, and penalizes the performance of coupled reactive transport simulations. In contrast, neural networks always need the same number of floating point operations per speciation calculation, thus providing an excellent condition for CPU-cores balancing in parallel simulations.

Through the example of Section 3.2, it has been demonstrated that a relatively small NN can provide excellent accuracy in a wide range of system compositions even after several hundreds of thousands of timesteps, which excludes the presence of systematic errors (Figs. 7–9). Another outcome of this study is the tradeoff of accuracy, robustness, compactness between the approaches using lookup tables and NN. For a low dimensional variable space with a limited range of parameters variability, the lookup table approach is preferred. A lookup table is straightforward to produce and to embed into a code as well. However,

for high dimensional problems with large parameter variations, the lookup table becomes impractical due to an exponential growth of the memory demand. For example, a lookup table with only 2 species, when represented on a 40 by 40 mesh, contains 1600 rows. A look up table with 6 species and same accuracy is consisted by more than four billion rows, posing severe memory and access time requirements. A NN has the potential to handle such a system with much lower computational and computer memory footprint, since fewer variables are needed to describe a neural network. Obviously, the training of such a network up to the desired accuracy is a very challenging task. The training of a NN at larger dimensions cannot be based on regular equidistant grids of the input variables since the sample basis would then be enormous. A possible approach would be to scan the multidimensional space in a probabilistic way for interesting regions and to locally refine the number of grid points.

Particularly promising is also the dynamic training of the NNs during the reactive transport simulation, which can be done in combination with full geochemical speciation solvers. On-the-fly trained NNs can be used to progressively accelerate the geochemical calculations by providing improved initial guesses for the chemical speciation calculations and eventually replace the chemical solver at the advanced simulation stage (Guérillot and Bruyelle, 2020). Once trained, the NN along with its specifications could be also deposited in an open database for further use from the scientific community. To this aim, the NN training packages could be interfaced with geochemical speciation codes and deliver the trained NNs as an externally linkable library for reactive transport simulation via a unified interface.

4.4. Significance of coupled reactive transport in geochemical applications and development of digital twins

Transient phenomena in complex multicomponent natural systems are particularly sensitive to the details of the process couplings (Steefel et al., 2005). The next challenge in coupled description of reactive transport processes at pore and continuum scale, is to consider the realistic description of heterogeneities in 3D. One of the major obstacles for the consideration of realistic geometries is the high computational overhead of the full speciation chemical solvers. A neural network based description of chemical equilibria seems at the moment to be an efficient and practical approach, enabling to address transient phenomena in high resolution 3D reactive transport simulations. For natural multicomponent systems, a more detailed analysis of the geochemistry may allow the identification of key processes controlling the system behavior. Such simulations are necessary for the accurate estimation of the critical time scales and the reaction pathways, for geochemical phenomena in natural and geo-engineered systems with strong geochemical gradients and non-linear coupling between chemical reactivity (ionic strength, pH, concentration of dominant species and solubility indexes

of key mineral phases), transport (porosity permeability diffusivity relationships) and heat transfer phenomena. Such systems include natural and engineered geothermal systems, carbon capture and storage, or disposal of nuclear waste.

Modern most advanced geochemical studies of fluid-mineral interaction show clear trends towards miniaturization of the experimental setup, process coupling and high resolution, often with *in situ* time resolved characterization of the processes. Such experiments deliver the data at an unprecedented level of detail and level of process complexity. Interpretation of the results require, however, full control on the experimental boundary condition and the process design. The accelerated multiscale reactive transport simulations offer a unique opportunity for the design, optimization, monitoring and eventually the active steering of miniaturized reactive transport experiments. A NN based digital twin of the experiment along with the augmented reality capabilities it offers (in-situ determination and prediction of chemical and flow conditions), will soon be an indispensable supplementary tool for the implementation of experimental high resolution reactive transport studies. Assuming that the geochemical speciation calculation is no more the computational bottleneck of the reactive transport modelling, it will be feasible to achieve real time simulation of the experimental conditions.

5. CONCLUSION

In this paper, we explore and benchmark the efficiency of NN framework to enhance reactive transport modelling. The selected applications are relevant to multiscale multiphysics modelling. The examples suggest that NNs can interface different codes that operate at a different length and time scale. For the reactive transport simulation, relevant to a lab-on-a-chip microfluidic experiment, the agreement between the NN implementation and the exact LMA solver for the calculation of the chemical speciation was excellent, with the NN performance being four orders of magnitude faster. The dynamic equilibrium of the system was controlled by advection, diffusion and mineral precipitation processes. The accuracy remained at high levels even after numerous computational time steps, despite the complexity of the involved mechanisms.

The NN clearly over perform full speciation reactive transport simulations and look-up table based approaches in terms of computational efficiency and memory demands. This performance comes at a price. Particular care has to be taken for the appropriate training of NN. Insufficient training or limited size of the training dataset in terms of the data volume and the coverage of the space of variables, may result in very poor accuracy of the NN.

Access to accurate and numerically efficient NNs opens horizons for large-scale 3D reactive transport simulations of complex natural systems, and further development of digital twins indispensable for experimental high resolution reactive transport studies. The success of such applications will depend very much on the efficiency and automation of NN training process for arbitrary problems.

Declaration of Competing Interest

ACKNOWLEDGEMENTS

APPENDIX A. SUPPLEMENTARY MATERIAL

Supplementary data to this article can be found online at https://doi.org/10.1016/j.gca.2020.07.019.

REFERENCES

Abadi M., Barham P., Chen J., Chen Z., Davis A., Dean J., Devin M., Ghemawat S., Irving G. and Isard M. (2016) Tensorflow: A system for large-scale machine learning. In *12th {USENIX} Symposium on Operating Systems Design and Implementation ({OSDI} 16)*, pp. 265–283.

Asher M. J., Croke B. F., Jakeman A. J. and Peeters L. J. (2015) A review of surrogate models and their application to groundwater modelling. *Water Resources Research* **51**, 5957–5973.

Bear J. (2013) *Dynamics of Fluids in Porous Media*. Courier Corporation.

Bijeljic B., Mostaghimi P. and Blunt M. J. (2013) Insights into non-Fickian solute transport in carbonates. *Water Resources Research* **49**, 2714–2728.

Burden F. and Winkler D. (2008) Bayesian regularization of neural networks. *Methods in Molecular Biology (Clifton N.J.)* **458**, 25–44.

Chen H., Kandasamy S., Orszag S., Shock R., Succi S. and Yakhot V. (2003) Extended Boltzmann kinetic equation for turbulent flows. *Science* **301**, 633–636.

Chopard, B., Kontaxakis, D., Lagrava, D., Latt, J., Malaspinas, O., Parmigiani, A., Rybak, T., Sagon, Y., 2015. The palabos project.

Christo F. C., Masri A. R. and Nebot E. M. (1996) Artificial neural network implementation of chemistry with pdf simulation of H-2/CO2 flames. *Combustion and Flame* **106**, 406–427.

Churakov S. V. and Gimmi T. (2011) Up-scaling of molecular diffusion coefficients in clays: A two-step approach. *Journal of Physical Chemistry C* **115**, 6703–6714.

Churakov S. V., Gimmi T., Unruh T., Van Loon L. R. and Juranyi F. (2014) Resolving diffusion in clay minerals at different time scales: Combination of experimental and modeling approaches. *Applied Clay Science* **96**, 36–44.

Churakov S. V. and Prasianakis N. (2018) Review of the current status and challenges for a holistic process-based description of mass transport and mineral reactivity in porous media. *American Journal of Science* **318**, 921–948.

Curti E., Xto J., Borca C. N., Henzler K., Huthwelker T. and Prasianakis N. I. (2019) Modelling Ra-bearing baryte nucleation/precipitation kinetics at the pore scale: application to radioactive waste disposal. *European Journal of Mineralogy M* **31**(2), 247–262.

De Lucia M., Kempka T., Jatnieks J. and Kuhn M. (2017) Integrating surrogate models into subsurface simulation framework allows computation of complex reactive transport scenarios. *Energy Procedia* **125**, 580–587.

Deng H., Steefel C., Molins S. and DePaolo D. (2018) Fracture evolution in multimineral systems: the role of mineral composition, flow rate, and fracture aperture heterogeneity. *ACS Earth and Space Chemistry* **2**, 112–124.

Gray F., Anabaraonye B., Shah S., Boek E. and Crawshaw J. (2018) Chemical mechanisms of dissolution of calcite by HCl in porous media: Simulations and experiment. *Advances in Water Resources.* **121**, 369–387.

Gruenberger A., Probst C., Heyer A., Wiechert W., Frunzke J. and Kohlheyer D. (2013) Microfluidic picoliter bioreactor for microbial single-cell analysis: fabrication system setup, and operation. *Journal of Visualized Experiments* **82**, 50560.

Guérillot D. and Bruyelle J. (2020) Geochemical equilibrium determination using an artificial neural network in compositional reservoir flow simulation. *Computational Geosciences* **24**, 697–707.

Heuveline V. and Krause M. J. (2010) *OpenLB: towards an efficient parallel open source library for lattice Boltzmann fluid flow simulations*. International Workshop on State-of-the-Art in Scientific and Parallel Computing, PARA.

Hoefner, M., Fogler, H.S., 1988. Pore evolution and channel formation during flow and reaction in porous media. AICHE Journal 34, 45–54.

Huang, Y., Shao, H., Wieland, E., Kolditz, O., Kosakowski, *Journal of Construction and Building Materials*, 2018. A new approach to coupled two-phase reactive transport simulation for long-term degradation of concrete. 190, 805-829.

Hubbard S. S., Williams K. H., Agarwal D., Banfield J., Beller H., Bouskill N., Brodie E., Carroll R., Dafflon B., Dwivedi D., Falco N., Faybishenko B., Maxwell R., Nico P., Steefel C., Steltzer H., Tokunaga T., Tran P. A., Wainwright H. and Varadharajan C. (2018) The East River, Colorado, Watershed: A mountainous community testbed for improving predictive understanding of multiscale hydrological-biogeochemical dynamics. *Vadose Zone Journal* **17**, 1–25.

Jain, A.K., Mao, J., Mohiuddin, K.M., 1996. Artificial neural networks: A tutorial. *Computer (IEEE)* 29, 31–44.

Jakob, A., Pfingsten, W., Van Loon, L., 2009. Effects of sorption competition on caesium diffusion through compacted argillaceous rock. *Geochimica et Cosmochimica Acta* 73, 2441–2456.

Jatnieks J., De Lucia M., Dransch D. and Sips M. (2016) Data-driven surrogate model approach for improving the performance of reactive transport simulations. *Energy Procedia* **97**, 447–453.

Kang, Q., Zhang, D., Chen, S., He, X., 2002. Lattice Boltzmann simulation of chemical dissolution in porous media. *Physical Review E*, **65**, 036318.

Kayri M. (2016) Predictive abilities of Bayesian regularization and levenberg-marquardt algorithms in artificial neural networks: A comparative empirical study on social data. *Mathematical and Computational Applications* **21**.

Kosakowski G. and Berner U. (2013) The evolution of clay rock/cement interfaces in a cementitious repository for low- and intermediate level radioactive waste. *Physics and Chemistry of the Earth* **64**, 65–86.

Kosakowski G. and Watanabe N. (2014) OpenGeoSys-Gem: A numerical tool for calculating geochemical and porosity changes in saturated and partially saturated media. *Phys. Chem. Earth, Parts A/B/C* **70–71**, 138–149.

Krüger, T., Kusumaatmaja, H., Kuzmin, A., Shardt, O., Silva, G., Viggen, E.M., 2017. The lattice Boltzmann method. *Springer International Publishing, Graduate Texts in Physics* 10, 978–3.

Kulik D. A., Wagner T., Dmytrieva S. V., Kosakowski G., Hingerl F. F., Chudnenko K. V. and Berner U. R. (2013) GEM-Selektor geochemical modeling package: revised algorithm and GEMS3K numerical kernel for coupled simulation codes. *Comput. Geosci.* **17**, 1–24.

Kurganskaya, I., Churakov, S.V., 2018. Carbonate dissolution mechanisms in the presence of electrolytes revealed by grand canonical and kinetic Monte Carlo modeling. *The Journal of Physical Chemicstry C*, 122, 29285–29297.

Laloy, E., Jacques, D., 2019. Emulation of CPU-demanding reactive transport models: a comparison of Gaussian processes, polynomial chaos expansion, and deep neural networks. *Computational Geosciences* 23 (5), 1193–1215.

Latt J., Malaspinas O., Kontaxakis D., Parmigiani A., Lagrava D., Brogi F., Belgacem M. B., Thorimbert Y., Leclaire S., Li S., Marson F., Lemus J., Kotsalos C., Conradin R., Coreixas C., Petkantchin R., Raynaud F., Beny J. and Chopard B. (2020) Palabos: Parallel Lattice Boltzmann Solver. *Comput. Math. Appl.*.

Leal, A.M., Kulik, D.A. and Saar, M.O., 2017a. Ultra-fast reactive transport simulations when chemical reactions meet machine learning: chemical equilibrium. *arXiv preprint arXiv:1708.04825*

Leal, A.M., Kulik, D.A., Smith, W.R., Saar, M.O., 2017b. An overview of computational methods for chemical equilibrium and kinetic calculations for geochemical and reactive transport modeling. *Pure and Applied Chemistry* 89, 597–643

Li L., Sanchez J. R., Kohler F., Røyne A. and Dysthe D. K. (2018) Microfluidic control of nucleation and growth of CaCO3. *Crystal Growth and Design.* **18**(8), 4528–4535.

Mackay D. J. C. (1992) Bayesian interpolation. *Neural Computation.* **4 (3)**, 415–447.

Marty, N.C., Claret, F., Lassin, A., Tremosa, J., Blanc, P., Madé, B., Giffaut, E., Cochepin, B., Tournassat, C., 2015. A database of dissolution and precipitation rates for clay-rocks minerals. *Applied Geochemistry* 55, 108–118.

Menke, H., Andrew, M., Blunt, M., Bijeljic, B., 2016. Reservoir condition imaging of reactive transport in heterogeneous carbonates using fast synchrotron tomography—Effect of initial pore structure and flow conditions. Chemical Geology **428**, 15–26

Mhaskar, H., Liao, Q., Poggio, T., 2016. Learning functions: when is deep better than shallow. arXiv preprint arXiv:1603.00988

Miller G. F., Todd P. M. and Hegde S. U. (1989) Designing neural networks using genetic algorithms. *In proceedings of the third international conference on Genetic Algorithms ICGA*, 379–384.

Molins S. and Knabner P. (2019) Multiscale approaches in reactive transport modeling. *Reviews in Mineralogy and Geochemistry* **85**, 27–48.

Molins S., Soulaine C., Prasianakis N. I., Abbasi A., Poncet P., Ladd A. J. C., Starchenko V., Roman S., Trebotich D., Tchelepi H. A. and Steefel C. I. (2020) Simulation of mineral dissolution at the pore scale with evolving fluid-solid interfaces: review of approaches and benchmark problem set. *Comput. Geosci.*, 1–34.

Molins S., Trebotich D., Steefel C. I. and Shen C. P. (2012) An investigation of the effect of pore scale flow on average geochemical reaction rates using direct numerical simulation. *Water Resour. Res.* **48**.

Montoya, V., Águila, J., Samper, J., Montenegro, L., Kosakowski, G., Krejci, P., Pfingsten, W., 2020. Modelling Cs migration through Opalinus clay: A benchmark for single-and multi-species sorption-diffusion models, *Proceedings of International Workshop on Geochemistry at HZDR, Dresden*, ISSN 2191-8708 (https://www.hzdr.de/publications/Publ-30921).

Noiriel C. and Daval D. (2017) Pore-scale geochemical reactivity associated with CO2 storage: New frontiers at the fluid-solid interface. *Acc. Chem. Res.* **50**, 759–768.

Panga M. K. R., Ziauddin M. and Balakotaiah V. (2005) Two-scale continuum model for simulation of wormholes in carbonate acidization. *AIChE J.* **51**, 3231–3248.

Parkhurst D. L. (1995) *User's Guide to PHREEQC: A Computer Program for Speciation, Reaction-path, Advective-transport, and Inverse Geochemical Calculations*. US Department of the Interior, US Geological Survey.

Parkhurst, D.L. and Appelo, C.J.W., 1999. User's guide to PHREEQC (Version 2): A computer program for speciation, batch-reaction, one-dimensional transport, and inverse geochemical calculations. 99, 312.

Patel R., Perko J. and Jacques D. (2017) Yantra: A lattice Boltzmann method based simulation tool for modelling physico-chemical processes in concrete at different spatial scales. In *XIV DBMC 14th International Conference on Durability of Building Materials and Components*, p. 335.

Patel, R.A., Perko, J., Jacques, D., De Schutter, G., Ye, G., Van Breugel, K., 2018. A three-dimensional lattice Boltzmann method based reactive transport model to simulate changes in cement paste microstructure due to calcium leaching. *Construction and Building Materials*, **166**, 158–170.

Pfingsten, W., 2002. Experimental and modeling indications for self-sealing of a cementitious low-and intermediate-level waste repository by calcite precipitation. *Nuclear Technology* 140, 63–82.

Poonoosamy J., Klinkenberg M., Deissmann G., Brandt F., Bosbach D., Mäder U. and Kosakowski G. (2020) Effects of solution supersaturation on barite precipitation in porous media and consequences on permeability, Experiments and modelling. *Geochimica et Cosmochimica Acta* **270**, 43–60.

Poonoosamy J., Westerwalbesloh C., Deissmann G., Mahrous M., Curti E., Churakov S. V., Klinkenberg M., Kohlheyer D., von Lieres E., Bosbach D. and Prasianakis N. I. (2019) A microfluidic experiment and pore scale modelling diagnostics for assessing mineral precipitation and dissolution in confined spaces. *Chem. Geol.* **528**.

Portier, S., Vuataz, F.-D., Nami, P., Sanjuan, B., Gérard, A., 2009. Chemical stimulation techniques for geothermal wells: experiments on the three-well EGS system at Soultz-sous-Forêts, France. *Geothermics* **38**, 349–359.

Prasianakis, N., Karlin, I., Mantzaras, J., Boulouchos, K., 2009. Lattice Boltzmann method with restored Galilean invariance. *Physical Review E* **79**, 066702.

Prasianakis, N., Rosén, T., Kang, J., Eller, J., Mantzaras, J., Büichi, F., 2013. Simulation of 3D porous media flows with application to polymer electrolyte fuel cells. *Communications in Computational Physics* **13**, 851-866.

Prasianakis N. I., Curti E., Kosakowski G., Poonoosamy J. and Churakov S. V. (2017) Deciphering pore-level precipitation mechanisms. *Scientific Reports* **7**, 13765.

Prasianakis N. I., Gatschet M., Abbasi A. and Churakov S. V. (2018) Upscaling strategies of porosity-permeability correlations in reacting environments from pore-scale simulations. *Geofluids*, 9260603–9260608.

Prasianakis, N.I., Karlin, I.V., 2008. Lattice Boltzmann method for simulation of compressible flows on standard lattices. *Physical Review E* **78**, 016704.

Rumelhart D. E., Hinton G. E. and Williams R. J. (1986) Learning representations by back-propagating errors. *Nature* **323**, 533–536.

Safi, M.A., Prasianakis, N., Turek, S., 2017a. Benchmark computations for 3D two-phase flows: A coupled lattice Boltzmann-level set study. *Computers and Mathematics with Applications* **73**, 520–536.

Safi M. A., Prasianakis N. I., Mantzaras J., Lamibrac A. and Buchi F. N. (2017b) Experimental and pore-level numerical investigation of water evaporation in gas diffusion layers of polymer electrolyte fuel cells. *Int. J. Heat Mass Transf.* **115**, 238–249.

Seigneur N., Mayer K. U. and Steefel C. I. (2019) Reactive transport in evolving porous media. *Rev. Mineral. Geochem.* **85**, 197–238.

Shen, C., Laloy, E., Elshorbagy, A., Albert, A., Bales, J., Chang, F.-J., Ganguly, S., Hsu, K.-L., Kifer, D., Fang, Z., 2018. HESS Opinions: Incubating deep-learning-powered hydrologic science advances as a community. *Hydrology and Earth System Sciences* **22** (11).

Song, W., de Haas, T.W., Fadaei, H., Sinton, D., 2014. Chip-off-the-old-rock: the study of reservoir-relevant geological processes with real-rock micromodels. *Lab on a Chip* **14**, 4382–4390.

Soulaine C., Roman S., Kovscek A. and Tchelepi H. A. (2017) Mineral dissolution and wormholing from a pore-scale perspective. *J. Fluid Mech.* **827**, 457–483.

Soulaine, C., Roman, S., Kovscek, A., Tchelepi, H.A., 2018. Pore-scale modelling of multiphase reactive flow: application to mineral dissolution with production of CO2. *J. Fluid Mech.* **855**, 616–645.

Starchenko V. and Ladd A. J. C. (2018) The development of wormholes in laboratory-scale fractures: perspectives from three-dimensional simulations. *Water Resour. Res.* **54**, 7946–7959.

Steefel C. I., Appelo C. A. J., Arora B., Jacques D., Kalbacher T., Kolditz O., Lagneau V., Lichtner P. C., Mayer K. U., Meeussen J. C. L., Molins S., Moulton D., Shao H., Simunek J., Spycher N., Yabusaki S. B. and Yeh G. T. (2015) Reactive transport codes for subsurface environmental simulation. *Comput. Geosci.* **19**, 445–478.

Steefel, C.I., DePaolo, D.J., Lichtner, P.C., 2005 Reactive transport modeling: An essential tool and a new research approach for the Earth sciences. *Earth and Planetary Science Letters* **240**, 539–558.

Succi S. (2001) *The Lattice Boltzmann Equation: For Fluid Dynamics and Beyond.* Oxford University Press.

Tölke, J., Krafczyk, M., 2008. TeraFLOP computing on a desktop PC with GPUs for 3D CFD. *International Journal of Computational Fluid Dynamics* **22**, 443–456.

Wersin P., Van Loon L. R., Soler J. M., Yllera A., Eikenberg J., Gimmi T., Hernan P. and Boisson J. Y. (2004) Long-term diffusion experiment at Mont Terri: first results from field and laboratory data. *Appl. Clay Sci.* **26**, 123–135.

Xu, T., Spycher, N., Sonnenthal, E., Zhang, G., Zheng, L., Pruess, K., 2011. TOUGHREACT Version 2.0: A simulator for subsurface reactive transport under non-isothermal multiphase flow conditions. 37, 763–774.

Yang G., Prasianakis N. I. and Churakov S. V. (2020) Comparative modeling of ions and solvent properties in Ca-Na montmorillonite by atomistic simulations and fluid density functional theory. *Clays Clay Miner.*.

Yang, Y., Patel, R.A., Churakov, S.V., Prasianakis, N.I., Kosakowski, G., Wang, M., 2019. Multiscale modeling of ion diffusion in cement paste: electrical double layer effects. *Cement and Concrete Composites* **96**, 55–65.

Yao, X., 1999. Evolving artificial neural networks. *Proceedings of the IEEE* **87** (9), 1423–1447.

Associate editor: Carl Steefel